Landslides (2019) 16:165–174
DOI 10.1007/s10346-018-1069-y
Received: 18 May 2018
Accepted: 25 September 2018
Published online: 22 October 2018

Federica Fiorucci · Francesca Ardizzone · Alessandro Cesare Mondini · Alessia Viero · Fausto Guzzetti

Visual interpretation of stereoscopic NDVI satellite images to map rainfall-induced landslides

Abstract Landslide inventory maps are commonly prepared through the visual interpretation of stereoscopic aerial photographs and field checks. Stereoscopic satellite images can also be interpreted visually to recognize and map landslides. When interpreting stereoscopic imagery, shadows can conceal the photographic elements typical of landslides, hampering the recognition and mapping of the landslides. To mitigate the problem, we propose a method that exploits normalized difference vegetation index (NDVI) images and digital stereoscopy for the 3D visual recognition and mapping of landslides in shadowed areas. We tested the method in the 25 km^2 Pogliaschina catchment, northern Italy, where intense rainfall caused abundant landslides on 25 October 2011. Using a PLANAR® StereoMirror™ digital stereoscope, we prepared an event landslide inventory map (E-LIM) through the visual interpretation of a pair of NDVI images obtained from a WorldView-2 stereoscopic multispectral bundle. We compared the event inventory with two independent E-LIMs for the same area and landslide event. The 3D vision of the NDVI stereoscopic image pair maximized the use of the radiometric (color and tone) and the terrain (elevation, slope, relief, and convexity) information captured by the stereoscopic multispectral images, allowing for the recognition of more landslides and more landslide areas than the other E-LIMs in the shadowed areas. Our results confirm that use of NDVI images facilitates the visual recognition and mapping of landslides in terrain affected by shadows. We expect that the proposed method can help trained interpreters to map landslides more accurately in areas affected by shadows.

Keywords Digital stereoscopic vision · Landslide inventory map · Normalized difference vegetation index · WorldView-2

Introduction

For decades, landslide inventory maps (LIMs) have been prepared through the visual interpretation of stereoscopic aerial photographs aided by field surveys. The growing availability of high and very high resolution satellite images is driving the experimentation of automatic and semi-automatic methods for landslide detection and mapping (Guzzetti et al. 2012). Today, monoscopic, panchromatic, and multispectral satellite images can be used to prepare projected and orthorectified images equivalent in quality to aerial orthophotographs (Casagli et al. 2005; Weirich and Blesius 2007; Marcelino et al. 2009; Fiorucci et al. 2011; Sun et al. 2017), or they can be combined with digital elevation models to obtain 3D views. Stereoscopic panchromatic and multispectral satellite images can also be used to prepare anaglyphs and stereoscopic models that can be interpreted visually to recognize and map landslides (Haeberlin et al. 2004; Nichol et al. 2006; Weirich and Blesius 2007; Bajracharya and Bajracharya 2008; Alkevli and Ercanoglu 2011; Ardizzone et al. 2013; Murillo-García et al. 2015).

The visual interpretation approach considers a set of photographic elements typical of landslides, including shape, size, color, tone, mottling, and texture (Rib and Liang 1978; van Zuidam 1985; Antonini et al. 2002; Guzzetti et al. 2012). Shadows are an additional element that can help—or hamper—the visual interpretation of aerial or satellite imagery (Hackman 1967; Philipson 1997; Moreno et al. 2008; Paine and Kiser 2012). Under favorable lighting conditions, features such as landslide scarps, lateral cracks, or pressure ridges can be recognized by their shadows. However, steep and rugged terrain shadows generated by low illumination angles can conceal the photographic elements typical of landslides, limiting or even preventing the effective visual interpretation of aerial or satellite imagery.

In this work, we propose a method that exploits normalized difference vegetation index (NDVI) images and 3D digital stereoscopy for the visual recognition and mapping of event landslides by trained investigators. We tested the method preparing an event landslide inventory map (E-LIM) for the Pogliaschina catchment, northern Italy, where on 25 October 2011, an intense rainfall event triggered numerous landslides (Marchi et al. 2013; Bartelletti et al. 2017), and we compared the new event inventory to two pre-existing E-LIMs available for the same area and the same event (Mondini et al. 2014).

Study area

The Pogliaschina torrent is a right tributary of the Vara River that drains a portion of the eastern Ligurian Apennines range into the Tyrrhenian Sea, in northern Italy (Fig. 1 a, b). In the 25-km^2 catchment, elevation ranges from 95 to 720 m (average, 340 m) and terrain slope from 0° to 63° (average, 28.5°), with local differences controlled by the geological and tectonic settings (Marchi et al. 2013). The area is characterized by the presence of a NW-SE regional thrust associated with high-angle normal faults. Carbonate rocks, overlaid by siltstones and mudstones pertaining to the Scaglia Toscana and the Macigno Formations, crop out W of the thrust, and carbonates and sandstones covered by ophiolites and turbidites pertaining to the Monte Gottero flysch crop out E of the thrust. Fluvial deposits, recent in age, mantle locally the Pogliaschina valley floor (Mondini et al. 2014; Bartelletti et al. 2017). Climate is Mediterranean, with dry summers and most of the precipitation falling as rainfall from October to November. Mean annual precipitation in the 50-year period 1961–2010 was 1500 mm, with a maximum of 2417.6 mm measured by the Brugnato rain gauge, at 115 m of elevation (Desiato et al. 2011). The landscape is mostly forested. Vineyards, olive groves, and agricultural areas cover about 10% of the catchment, and urban areas are small and concentrate at lower elevations.

Landslides are abundant in the catchment, and are represented by rotational and translational slides, earthflows, soil slips, debris flows, and compound landslides (Marchi et al. 2013). On 25

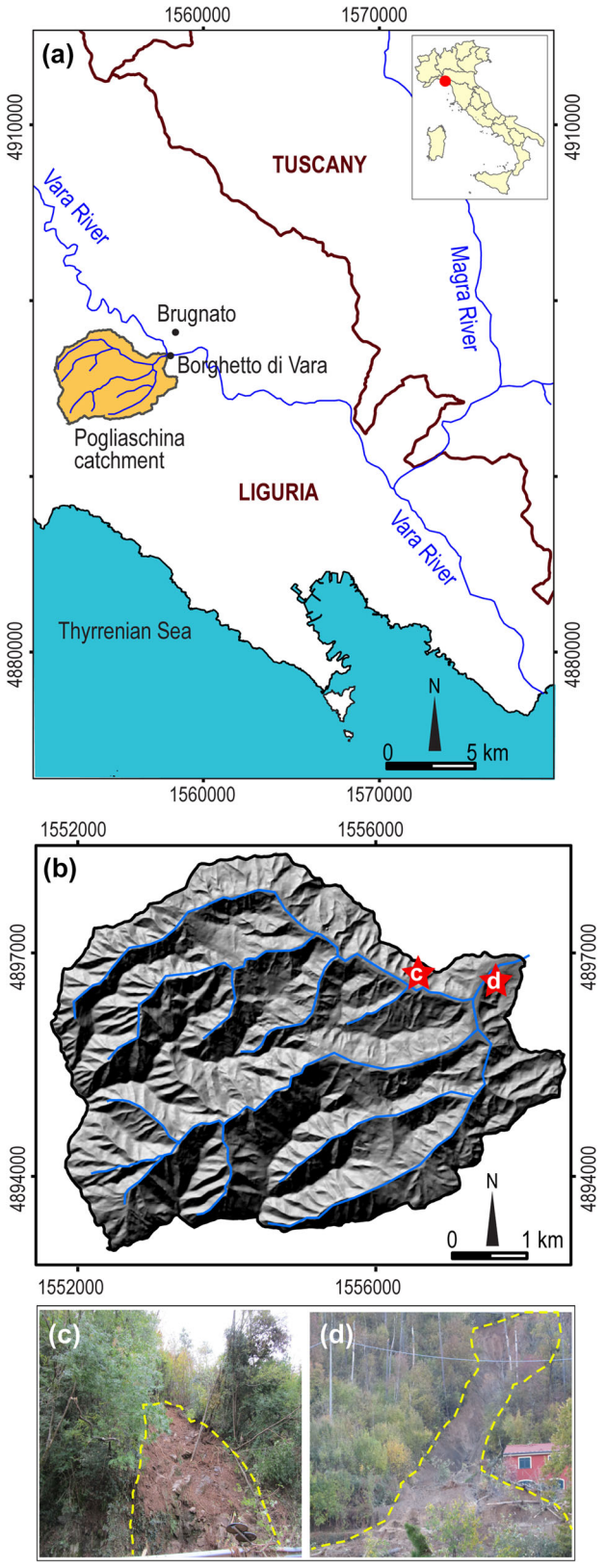

Fig. 1 **a** Index map showing geographical location of the Pogliaschina catchment (orange area), Liguria, northern Italy. **b** Shaded relief image showing topography in the Pogliaschina catchment. Blue lines show drainage network. Red stars show location of two landslides caused by intense rainfall on 25 October 2011, shown by dashed yellow lines in (**c**) and (**d**)

October 2011, an intense rainstorm hit the Tyrrhenian coast between Liguria and Tuscany. In Val di Vara, rainfall intensity exceeded 150 mm h^{-1}, and the Brugnato rain gauge measured 539 mm of rainfall in 24 h. The intense rainfall triggered numerous landslides, mostly soil slips and earthflows (Fig. 1 c, d) and caused a flash flood along the Pogliaschina torrent (Marchi et al. 2013).

Data

Satellite imagery

A pair of the WorldView-2 stereoscopic satellite images of the study area taken on 29 October 2011—4 days after the landslide-triggering rainfall event—in panchromatic and multispectral bands was available to us. The image pair has a 0.5-m ground sampling distance (GSD) in the panchromatic band and a 2-m GSD in the multispectral bands (blue, green, red, near-infrared regions (NIR)). The two images were acquired with off-nadir angles of 6.6° and 32.2°, and made available to us in the WGS84 coordinate system. Due to the local morphological setting (Fig. 1b) and the date of the acquisition, in mid-autumn, 32% of the stereoscopic-pair is affected by shadows that reduce the illumination of many of the NW-facing slopes (Mondini et al. 2014).

Landslide event inventory maps

Two pre-existing E-LIMs showing landslides triggered by the 25 October 2011 rainfall event were available (Mondini et al. 2014). The first event inventory (MAP A in Fig. 2 a, b) was obtained through the visual interpretation of (i) post-event aerial photographs and orthophotographs, for 62.5% of the study area and of (ii) the panchromatic WorldView-2 stereoscopic image, for the remaining 37.5% of the area. The visual interpretation of the aerial and the satellite imagery was aided by field surveys conducted to resolve local ambiguities (Mondini et al. 2014). MAP A shows 591 landslides, corresponding to a density of 23.6 landslides per km², for a total landslide area A_{LT} = 452,079 m². In the E-LIM, the smallest landslide has A_L = 11 m², the largest landslide has A_L = 13,795 m², and the average landslide area is $\hat{A}_L$ = 764 m² (Table 1).

The second event inventory (MAP B in Fig. 2 c, d) was prepared using a semi-automatic classification procedure applied to the WorldView-2 multispectral bundle (Mondini et al. 2014). MAP B shows 537 landslides, corresponding to a density of 21.5 landslides per km², for a total landslide area A_{LT} = 382,931 m². In this E-LIM, the smallest landslide has A_L = 31 m², the largest landslide has A_L = 7869 m², and the average landslide area is $\hat{A}_L$ = 713 m² (Table 1).

The two E-LIMs (MAP A and MAP B) were compared to a new event inventory prepared in this study (MAP C in Fig. 2 e, f), which we present in the "Results" section.

Method

We propose a method to facilitate trained investigators to recognize and map landslides in shadowed areas. The method exploits NDVI images prepared to improve the information given to a photo interpreter for the heuristic, visual recognition of event landslides using 3D digital stereoscopy. This is obtained in four steps (Fig. 3), which include (i) the preparation of standard NDVI images from stereoscopic multispectral satellite images; (ii) the contrast enhancement of the NDVI images, if necessary; (iii) the preparation of a stereoscopic model of the (enhanced) NDVI

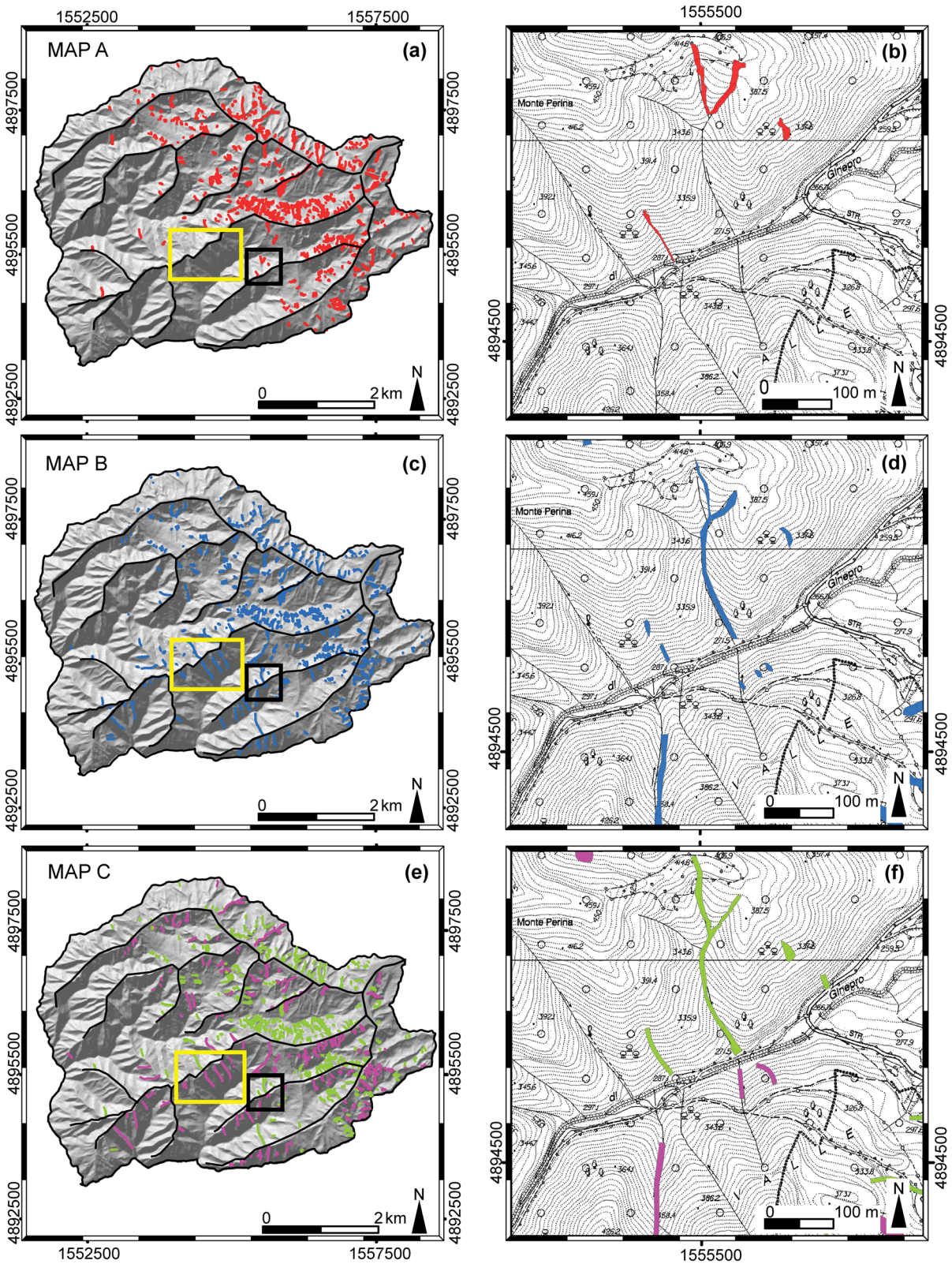

Fig. 2 Event landslide inventory maps (E-LIMs) for the Pogliaschina catchment, northern Italy, used in this study. **a**, **c**, **e** Show inventories for the entire study area. Black rectangles show location of panels (**b**), (**d**), and (**f**) that portray enlarged maps for a small portion of the study area. MAP A (upper row) shows E-LIM prepared by visual interpretation of post-event aerial photographs, orthophotographs, and the panchromatic WorldView-2 stereoscopic images, aided by field surveys (Mondini et al. 2014). Landslides are shown in red. MAP B (middle row) shows E-LIM prepared using a semi-automatic procedure applied to the multispectral bundle acquired by the WorldView-2 satellite (Mondini et al. 2014). Landslides are shown in blue. MAP C (lower row) shows E-LIM prepared in the study through the visual interpretation of e-NDVI^{100} stereoscopic pair obtained from the WorldView-2 satellite images. Landslides are shown in green in areas not affected by shadows and in violet in areas affected by shadows. Yellow rectangles show location and extent of area shown in Fig. 4

Table 1 Descriptive statistics for three event landslide inventory maps (E-LIMs) (Fig. 2) available for the Polgliaschina catchment and used in this study

	MAP A	MAP B	MAP C
Number of mapped landslides (n)	591	537	551
Landslide density (n/km^2)	23.64	21.48	22.04
Minimum landslide area (m^2)	11	31	44
Maximum landslide area (m^2)	13,795	7869	9033
Mean landslide area, $\hat{A}_L$ (m^2)	764	713	904
Total landslide area, A_{LT} (m^2)	452,079	382,931	498,230

MAP A, E-LIM prepared by Mondini et al. (2014) through the visual interpretation of aerial and satellite imagery, aided by field surveys

MAP B, E-LIM prepared by Mondini et al. (2014) exploiting a semi-automatic classification procedure applied to a multispectral WorldView-2 satellite image

MAP C, E-LIM prepared in this work through the 3D digital visual interpretation of contrast-enhanced e-NDVI images obtained from a WorldView-2 stereoscopic multispectral image pair

images for 3D visualization; and (iv) the visual analysis of the 3D stereoscopic model for landslide recognition and mapping, and the preparation of an E-LIM.

Preparation of the NDVI image pair

The first phase of the method (I in Fig. 3) consists in the calculation of the normalized difference vegetation index, NDVI $= \frac{NIR-R}{NIR+R}$, where R and NIR are the spectral radiance measurements acquired in the red (R) and the near-infrared (NIR) regions, for the single multispectral images of the stereoscopic pair. For this step, we used ERDAS IMAGINE® software that produced for each image a matrix of real (floating point) numbers in the range from − 1.0 to + 1.0. Our 3D-visualization system used for the interpretation of the stereoscopic images did not accept images represented by floating point numbers. For this reason, we transformed the original NDVI values to obtain NDVI^{100} = INT (100 × NDVI).

Figure 4a shows a panchromatic view of a portion of the study area where rainfall-induced landslides occurred on 25 October 2011. The landslides are not visible in the image, due to the presence of shadows that conceal the landslide features. Figure 4b shows the NDVI^{100} image for the same area. The event landslides present in the area are visible in the NDVI^{100} image, allowing the interpreter to recognize and map them, albeit with some difficulty.

Enhancement of the NDVI image pair

The second phase (II in Fig. 3) enhances the contrast of the NDVI^{100} image pair. This step is optional, and is performed if (or where) the contrast of the NDVI^{100} image is low. Contrast, the ratio between the difference and the sum of the maximum and the minimum luminescence values in an image, $C = \frac{L_{max}-L_{min}}{L_{max}+L_{min}}$ (Barten 1999), is key to the visual recognition of objects (Brivio et al. 2006). Where contrast is low, it may be difficult, or even impossible, for an interpreter to discriminate an object (i.e., a landslide) from the surrounding (i.e., the non-landslide area). For digital images, contrast can be enhanced using a variety of techniques that operate in the image frequency or spatial domains (Maini and Aggarwal 2010; Bedi and Khandelwal 2013). In our test case, to enhance the low contrast images (Fig. 4b), we used the "piecewise linear contrast stretch" technique available in ERDAS IMAGINE® software. Figure 4c shows the result of the image stretching. In the contrast-enhanced image, the narrow event landslides are more clearly visible than in the low contrast image, making it simpler for the interpreter to recognize and map the event landslides.

E-NDVI^{100} stereoscopic model for 3D visualization

The third phase (III in Fig. 3) consists in the preparation of a stereoscopic model of the contrast-enhanced, e-NDVI^{100} image pair for 3D visual interpretation. The step involves first the internal and the external orientations of the image pair. For the purpose, we used ERDAS IMAGINE Photogrammetry® software. For the internal orientation, we used the geometric information on the sensor model (SM) provided by the software for the WorldView-2 satellite, and for the external orientation, we used the information in the rational polynomial coefficients (RPC) file associated to the multispectral image bundle.

Next, to obtain a 3D view of the e-NDVI^{100}-oriented image pair, we used a PLANAR® StereoMirror™ system (http://www.planar.com/media/211324/mn-planar-sd2020.pdf). The digital display system exploits two active matrix liquid crystal display (AC-LCD) monitors oriented at an angular distance of 110°. A passive beam splitter mirror bisects the angle between the two monitors. The laterally reversed right image is projected on the top screen, and the left image is projected on the bottom (front) screen. Using passive polarization glasses, a photo interpreter sees the right image reflected on the mirror with the right eye, and the left (frontal) image with the left eye. Fusion of the right and left images in the photo interpreter's brain allows for the 3D visualization of the contrast-enhanced e-NDVI^{100}-oriented image pair (Fig. 5).

Visual interpretation of the 3D stereoscopic model

The last phase of the method (IV in Fig. 3) consists in the 3D visual analysis of the oriented pair of contrast-enhanced e-NDVI^{100} stereoscopic images, allowing a trained interpreter to recognize and map the event landslides captured by the satellite image pair. This is equivalent to what a photo interpreter does when he/she interprets visually a pair of stereoscopic aerial photographs using an analog or digital stereoscope. For this step, we used Stereo Analyst for ArcGIS® software that allowed the interpreter to recognize the event landslides and to draw the landslide geometry directly on the 3D-view. The geographic and geometric information on the event landslides was stored in a GIS database for further processing and analysis. The process reduced the acquisition time and the errors associated with the manual transfer of the landslide information from the image to a digital map (Santangelo et al. 2015).

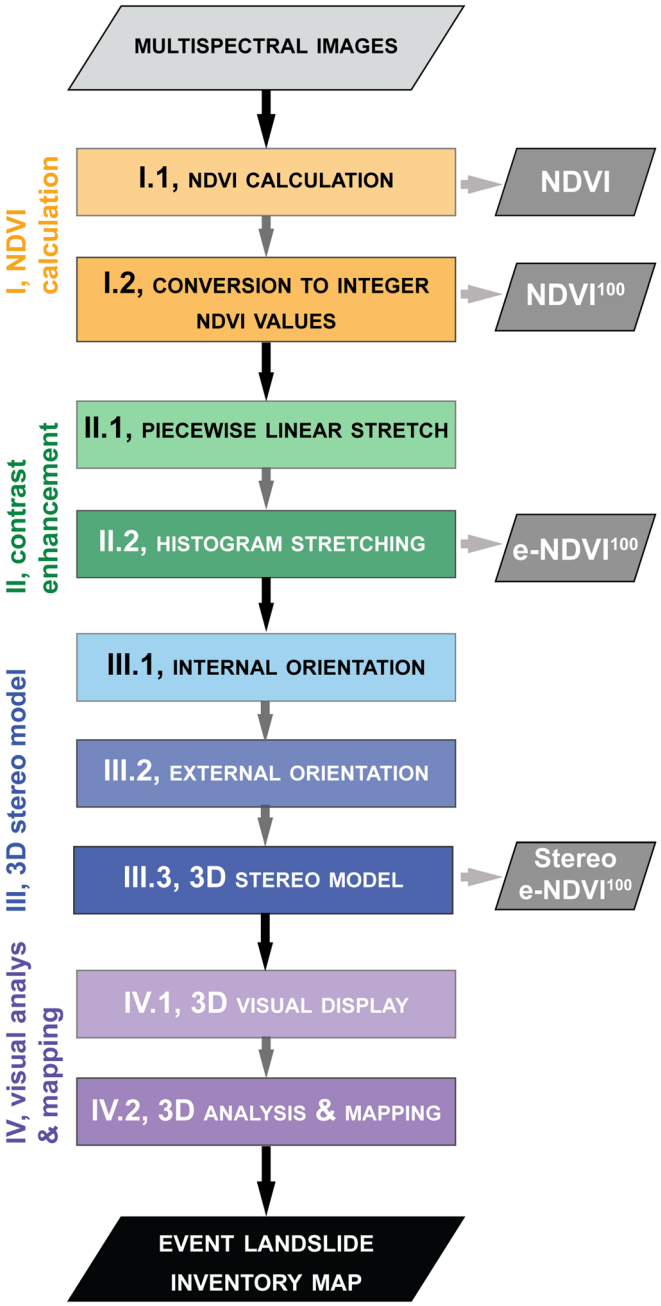

Fig. 3 Logical framework for the method proposed to exploit normalized difference vegetation index (NDVI) images and 3D digital stereoscopy for the visual recognition and mapping of event landslides in areas affected by shadows. Colored rectangles show model steps in four phases. Parallelograms show input (top), intermediate outputs (right), and output (bottom) products. See text for explanation

In places, visual mapping of the event landslides proved difficult due to the large parallax—the distance between two corresponding points—in the image pair. Parallax is responsible for the apparent displacement of an object viewed from different lines of sight, and conditions the effective interpretation of landslides and other geomorphological features. The two satellite images had a large difference in their off-nadir angles (6.6° and 32.2°), making parallax control problematic. In places, mapping small and elongated landslides proved difficult,

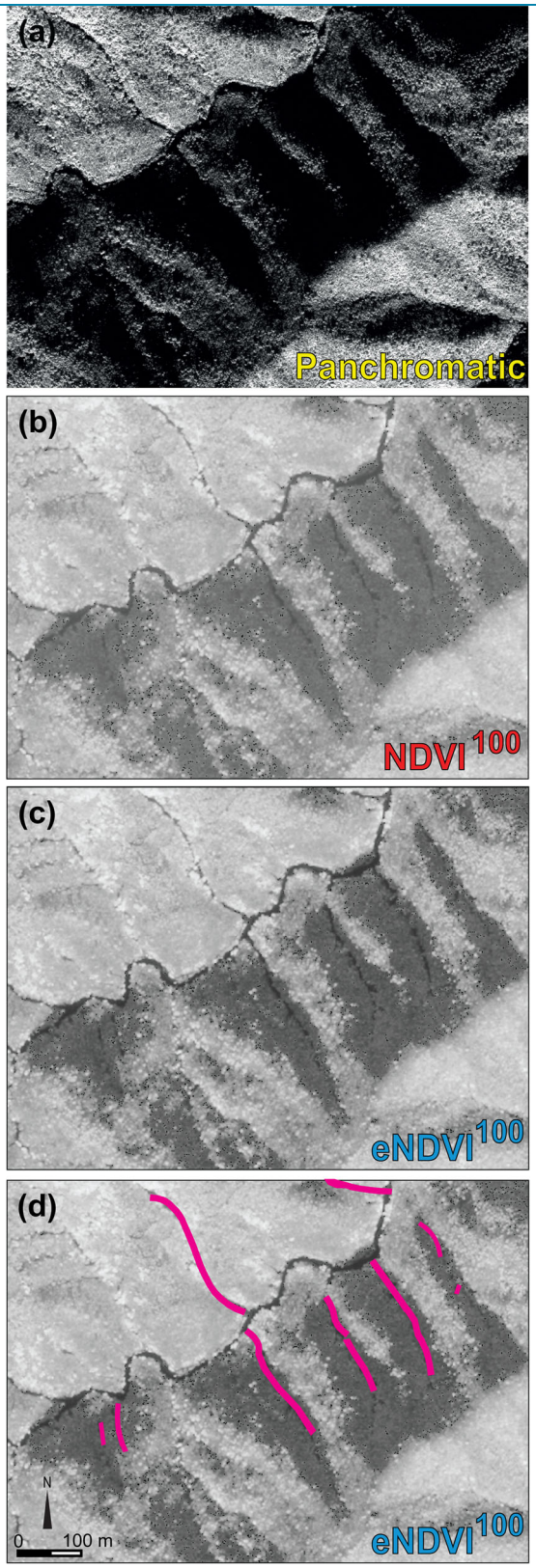

Fig. 4 Example of the application of the proposed method for a portion of the study area. **a** Original, panchromatic satellite image. **b** Re-scaled normalized difference vegetation index, $NDVI^{100}$ image. **c** Contrast-enhanced $e\text{-}NDVI^{100}$ image. **d** Same as (c) with mapped event landslides (in violet). See yellow rectangles in Fig. 2 for location of the area in the Pogliaschina catchment

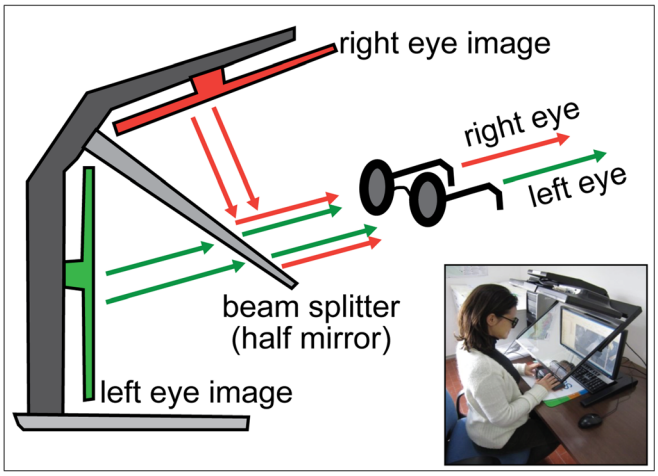

Fig. 5 Illustrative sketch of the PLANAR® StereoMirror™ digital system used in the study for the stereoscopic visualization of the contrast-enhanced e-NDVI^{100}-oriented image pair

particularly in steep, narrow channels where it was not easy to keep the floating cursors of the PLANAR® system on the topographic surface. To cope with the problem, we mapped the small and elongated landslides in steep and narrow channels as lines. Next, we buffered the lines to obtain polygons to represent the landslides, with the size of the buffer selected from measurements of the width of the channels (from 3 to 23 m, mean = 8 m, $\sigma = 2.8$ m), also obtained from the satellite images.

Results

We used the contrast-enhanced e-NDVI^{100} 3D stereoscopic model prepared adopting the method described in the "Method" section to recognize visually and map digitally the rainfall-induced event landslides triggered by the 25 October 2011 rainfall event in the Pogliaschina catchment. The new E-LIM, shown as MAP C in Fig. 2e, has 551 landslides (Table 1), corresponding to a density of 22.0 landslides per km^2. The figures include 386 landslides in steep terrain and narrow channels that were mapped as lines and buffered to obtain the corresponding landslide polygon. The total landslide area in MAP C is $A_{LT} = 498{,}230$ m^2. In the new event inventory, the smallest landslide has $A_L = 44$ m^2, the largest landslide has $A_L = 9033$ m^2, and the average landslide area is $\hat{A}_L = 904$ m^2 (Table 1).

We compared MAP C prepared in this work to the two previous E-LIMs available for the study area, i.e., MAP A showing 591 landslides and MAP B showing 537 landslides caused by the 25 October 2011 rainfall event (Mondini et al. 2014) (Fig. 2). The comparison revealed that the three E-LIMs are different in terms of the number of the mapped landslides and of the statistics of the landslide areas (Table 1). The comparison revealed a small difference between MAP A and MAP B, as shown by Mondini et al. (2014), with MAP A showing 9.1% more landslides and 15.3% more landslide area than MAP B. A smaller difference exists between MAP A and MAP C, with MAP A showing 6.7% more landslides than MAP C, whereas MAP C shows 9.2% more landslide area than MAP A. MAP C has 2.5% more landslides and 23.1% more landslide area than MAP B (Table 1).

Considering only the shadowed areas (Table 2) and counting the number of landslides and the total landslide area A_{LT}, the main differences are for landslides recognized using the satellite images and the orthophotographs (MAP A). Table 2 shows that in the shadowed areas, MAP A is substantially different from both MAP B and MAP C, whereas MAP B and MAP C show similar number of landslides and comparable A_{LT}. In the shadowed areas, MAP C has 20.7% more landslides and 23.5% more landslide area than MAP B. Considering the non-shadowed areas, the number of landslides, and the total landslide area A_{LT}, the main differences are for the landslides recognized using the satellite images and the orthophotographs (MAP A). Table 2 shows that MAP A is substantially different from both MAP B and MAP C, whereas MAP B and MAP C show similar number of landslides and a comparable A_{LT}. In the non-shadowed areas, MAP B has 5.8% more landslides and MAP C has 22.8% more landslide area than MAP B.

To quantify the degree of spatial match between the three E-LIMs, we computed the mismatching index, E (Carrara et al. 1992) and the related matching index, M (Galli et al. 2008),

$$M = 1 - E,\ E = \frac{\left(A^1_{LT} \cup A^2_{LT}\right) - \left(A^1_{LT} \cap A^2_{LT}\right)}{\left(A^1_{LT} \cup A^2_{LT}\right)};\ 0 \le M \le 1,\ 0 \le E \le 1,$$

where A^1_{LT} and A^2_{LT} are the total landslide areas of two landslide inventories, and $\cup$ and $\cap$ are the geometric union and intersection of the inventories. Where two maps show exactly the same landslides in the same geographical locations, the degree of matching is perfect ($M = 1$), and the mapping error is null ($E = 0$). Where instead the maps show landslides in completely different locations, the cartographic matching is null ($M = 0$), and the mapping error is maximum ($E = 1$). Using the three E-LIMs shown in Fig. 2 (MAP A, MAP B, and MAP C), we calculated the E and M indices for all the map pairs (Table 3). We calculated the indices considering (i) the entire study area (25 km^2), (ii) the portion of the study area affected by shadows (~ 8 km^2), and (iii) the portion of the study area not affected by shadows (~ 17 km^2). The results confirm that the three inventories are different.

To compare the spatial distribution of landslides in the three E-LIMs, we further examined the spatial correlation between pairs of inventory maps (Mondini et al. 2014). We first applied to E-LIM pairs a diversity filter to reduce the co-registration errors. The filter consisted in a kernel, 7 × 7 pixel in size, moved across pairs of landslide maps. The filtering process resulted in three diversity maps, and we determined the spatial correlation between the pairs of the diversity maps computing their correlation coefficient,

$$cc_{\rho 1 \rho 2} = \frac{\mathrm{cov}(\rho 1, \rho 2)}{\sigma_{\rho 1 \rho 2}},$$

where, ρ_1 and ρ_2 are the two spatial landslide diversity maps, cov is the corresponding covariance matrix, and $\sigma_{\rho 1}$ and $\sigma_{\rho 2}$ are the standard deviations of ρ_1 and ρ_2, respectively. Values of $cc_{\rho 1 \rho 2}$ close to 1 indicate a high level of similarity between the maps, and values of $cc_{\rho 1 \rho 2}$ close to 0 indicate a low similarity of the maps (Mondini et al. 2014). We computed the correlation coefficients for the three pairs of density maps obtained from the E-LIMs considering three cases: (i) the entire study area (25 km^2); (ii) the sub-area affected by shadows (~ 8 km^2, 32%), where the visual recognition of the event landslides was more problematic; and (iii) the portion of the

Table 2 Statistics for the three E-LIMs in areas affected (~ 8 km^2, 32% of the total area) and the not affected (~ 17 km^2, 68%) by shadows

	MAP A	MAP B	MAP C
Number of mapped landslides (n)			
Shadowed areas	50	142	179
Non-shadowed areas	541	395	372
Density (n/km^2)			
Shadowed areas	6.25	17.75	22.37
Non-shadowed areas	31.82	23.23	21.88
Minimum landslide area (m^2)			
Shadowed areas	126	78	56
Non-shadowed areas	10	31	44
Maximum landslide area (m^2)			
Shadowed areas	8191	7869	9033
Non-shadowed areas	13,795	5709	8175
Mean landslide area (m^2)			
Shadowed areas	1686	1283	1330
Non-shadowed areas	680	508	699
Total landslide area (m^2)			
Shadowed areas	84,300	182,322	238,153
Non-shadowed areas	367,778	200,610	260,077

MAP A, E-LIM prepared by Mondini et al. (2014) through the visual interpretation of aerial and satellite imagery, aided by field surveys

MAP B, E-LIM prepared by Mondini et al. (2014) exploiting a semi-automatic classification procedure applied to a multispectral WorldView-2 satellite image

MAP C, E-LIM prepared in this work through the 3D digital visual interpretation of contrast-enhanced e-NDVI images obtained from a WorldView-2 stereoscopic multispectral image pair

study area not interested by shadows (~ 17 km^2, 68%). The results revealed that MAP B and MAP C exhibit the largest similarity in all the considered cases (Table 4).

Discussion

The heuristic, visual interpretation of stereoscopic, aerial or satellite images remains a valuable and effective technique to map landslides over large and very large areas (Guzzetti et al. 2012). However, due to geometry of the acquisition, the date and time of the acquisition (that controlled the height and position of the sun), and the morphology of the terrain, the aerial and the satellite images are affected by shadows locally. The problem is particularly severe in the mountains and the hills, where terrain is rugged and slopes are steep. The presence of shadows hampers, and in places prevents, the visual recognition and mapping of landslides (Fig. 4). When working with analogic aerial photographs, the impact of shadows is unavoidable. Where shadows are dark, landslide mapping becomes inaccurate or incomplete, affecting the quality of the resulting LIMs.

Multispectral satellite (or aerial) images have more radiometric information than the traditional analogic, panchromatic, or color aerial photographs. Properly treated, the additional information can facilitate the visual recognition and mapping of landslides by a trained investigator in areas affected by shadows. Among the many spectral band ratio indices used in remote sensing to treat the complex information provided by multispectral images, the normalized difference vegetation index (NDVI) is known to be little sensitive to local topographic and illumination conditions (Lillesand et al. 1994; Lawrence and Ripple 1998) and to facilitate the visual recognition of landslides (Temesgena et al. 2001; Lee 2005; Hsieh et al. 2011; Schlögel et al. 2013; Liu 2015; Plank et al. 2016). Our work confirmed that use of stereoscopic NDVI images facilitates the visual recognition and mapping of landslides in rugged terrain affected by shadows.

For optimal results, the visual interpretation of aerial photography for landslide and geomorphological mapping (Rib and Liang 1978; van Zuidam 1985; Antonini et al. 2002; Guzzetti et al. 2012) is performed using stereoscopic vision, which allows a trained investigator to exploit jointly the photographic (e.g., color, tone, mottling, and texture) and the terrain (e.g., elevation, slope, relief, and convexity) information available from analogic aerial photography. In this work, we extended the use of the 3D vision to contrast-enhanced NDVI images, maximizing the use of the radiometric and the terrain information captured by the satellite stereoscopic pair. Results proved successful, with more landslides mapped in the shadowed areas (Table 2). We conclude that the proposed method can be used effectively to help a trained investigator to recognize and map landslides in areas affected by shadows.

We further note that calculation of the NDVI reduced the resolution of the images used for the visual interpretation from GSD = 0.5 m of the panchromatic image to GSD = 2.0 m. Despite the loss in resolution, the interpreter was able to map more landslides in the shadowed areas than the landslides shown in the other available inventories (Table 2). We take this as an indication of the fact that the joint use of stereoscopy and

Table 3 Mismatching (E) and matching (M) indices calculated for (I) the entire study area (25 km^2), (II) the area affected by shadows (~ 8 km^2, 32% of the area), and (III) the area non-affected by shadows (~ 17 km^2, 68%) for the three pairs of E-LIMs

I, Entire study area						
	MAP A		MAP B		MAP C	
	E	M	E	M	E	M
MAP AA	–	–	0.74	0.26	0.83	0.17
MAP B	0.74	0.26	–	–	0.70	0.30
MAP C	0.83	0.17	0.70	0.30	–	–
II, Areas affected by shadows						
	MAP A		MAP B		MAP C	
	E	M	E	M	E	M
MAP A	–	–	0.74	0.26	0.83	0.17
MAP B	0.74	0.26	–	–	0.70	0.30
MAP C	0.83	0.17	0.70	0.30	–	–
III, Illuminated areas without shadows						
	MAP A		MAP B		MAP C	
	E	M	E	M	E	M
MAP A	–	–	0.70	0.30	0.76	0.24
MAP B	0.70	0.30	–	–	0.68	0.32
MAP C	0.76	0.24	0.68	0.32	–	–

MAP A, E-LIM prepared by Mondini et al. (2014) through the visual interpretation of aerial and satellite imagery, aided by field surveys

MAP B, E-LIM prepared by Mondini et al. (2014) exploiting a semi-automatic classification procedure applied to a multispectral WorldView-2 satellite image

MAP C, E-LIM prepared in this work through the 3D digital visual interpretation of contrast-enhanced e-NDVI images obtained from a WorldView-2 stereoscopic multispectral image pair

NDVI images can be very effective to map landslides in hilly or mountain terrain areas affected by shadows. Further enhancements, not tested in this work, would be to experiment with pan-sharpening techniques (Mondini et al. 2011) to preserve in a higher resolution "sharpened" image (GSD = 0.5 m) the NDVI information available at a lower resolution (GSD = 2.0 m) or to experiment adaptive stretching of the panchromatic images. We expect that this could further enhance the ability of the investigator to map landslides accurately.

The availability of independent E-LIMs for the same event and the same area (Mondini et al. 2014) allowed for a quantitative comparison. The inventory map obtained through the visual interpretation of the available post-event aerial photographs, orthophotographs, and panchromatic WorldView-2 stereoscopic images (MAP A) shows more landslides than (i) the E-LIM prepared exploiting a semi-automatic procedure applied to the WorldView-2 satellite image (MAP B) and (ii) the E-LIM prepared in this work through the visual interpretation of the contrast-enhanced e-NDVI^{100} WorldView-2 stereoscopic satellite image pair (MAP C). In the areas affected by shadows (32% of the study area), MAP A has the lowest number of landslides (50), whereas MAP B (142) and MAP C (179) show a relatively similar number of landslides. MAP C has 37 more landslides and the largest total landslide area, A_{LT} = 238,153 m^2. We attribute this result to a better recognition and mapping of event landslides under the forest canopy in the shadowed areas, better exploiting the 3D radiometric and terrain information available from the

Table 4 Correlation coefficient cc_{p1p2} (Mondini et al. 2014) calculated for the three pairs of landslide density maps for the entire study area and for the portion of the study area affected by shadows

	Entire area	Shadowed areas	Non-shadowed areas
cc_{papb}	0.49	0.67	0.49
cc_{papc}	0.41	0.59	0.40
cc_{pbpc}	0.58	0.71	0.58

The three density maps were obtained using a low-Gaussian filter from the three E-LIMS (Fig. 2)

MAP A, E-LIM prepared by Mondini et al. (2014) through the visual interpretation of aerial and satellite imagery, aided by field surveys

MAP B, E-LIM prepared by Mondini et al. (2014) exploiting a semi-automatic classification procedure applied to a multispectral WorldView-2 satellite image

MAP C, E-LIM prepared in this work through the 3D digital visual interpretation of contrast-enhanced e-NDVI images obtained from a WorldView-2 stereoscopic multispectral image pair

stereoscopic multispectral images. We note that the effect was more relevant for narrow, channeled landslides.

We calculated the mismatch index *E* in a pairwise fashion for the entire study area, for the shadowed areas, and for the portion of the territory not covered by shadows (Table 4). Analysis of the mismatch indices confirmed that the differences between the three E-LIMs are significant, but in the range of differences measured by other investigators that have performed similar map comparisons (Carrara et al. 1992; Galli et al. 2008; Fiorucci et al. 2011). Comparison of the maps prepared exploiting the spectral information (semi-automatic classification in MAP B and visually interpreted e-NDVI images in MAP C), and the traditionally interpreted MAP A, revealed a higher mismatch in the shadowed areas, whereas the maps prepared exploiting the spectral information showed similar results in all areas. We conclude that effective use of the spectral information is important for the detection and mapping of landslides, particularly in the areas affected by shadows, where the visual interpretation of the standard optical aerial or satellite images is more difficult and error prone.

Lastly, we note that part of the mismatch revealed by the tests performed might be the result of a locally non-optimal co-registration of the satellite imagery. The effect is more relevant in steep terrain, and it is a consequence of the large difference in the off-nadir angles between the two satellite images and to the different resolutions of the satellite and the aerial imagery.

Conclusions

To mitigate the problem posed by shadows to the visual recognition of landslides from stereoscopic imagery, we proposed a method that exploits normalized difference vegetation index (NDVI) images and 3D digital stereoscopy to facilitate event landslide mapping by trained investigators. We tested the method using a pair of WorldView-2 stereoscopic multispectral images taken over the Pogliaschina catchment, NW, Italy (Fig. 1), 4 days after the 25 October 2011 landslide-triggering rainfall event (Marchi et al. 2013; Mondini et al. 2014). For each image in the stereoscopic pair, we prepared separate NDVI images at 2-m resolution, and we used a PLANAR® StereoMirror™ digital stereoscopic system (Fig. 5) to visualize a stereoscopic model of the NDVI image pair and to map the rainfall-induced landslides. We then compared the obtained event landslide inventory map (E-LIM) with two E-LIMs prepared independently for the same area and rainfall event (Mondini et al. 2014) (Fig. 2). Results proved the effectiveness of the proposed method, which in shadowed terrain allowed to map more landslides and more landslide area than the other E-LIMs. We attribute the improvement in the mapping to the stereoscopic vision of the NDVI images, which maximized the use of the radiometric (color and tone) and the terrain (elevation, slope, relief, and convexity) information captured by the multispectral pair. We expect that the proposed method will help trained investigators to map event landslides more accurately in areas affected by shadows, producing more complete landslide inventory maps. We further expect the method to be improved adopting pan-sharpening techniques or adaptive stretching of the panchromatic images.

Software and hardware used

For our experiment, we used a PLANAR® StereoMirror™ system, version 9.3.1; ERDAS IMAGINE Photogrammetry® software, version 10.1; and Stereo Analyst for ArcGIS® software, version 9.3.1.

Funding information This work was supported by the EU LAMPRE project (EC contract no. 312384). Federica Fiorucci was supported by a grant of the Regione dell'Umbria under contract PoR-FESR 861, 2012.

Compliance with ethical standards

Disclosure Any use of trade, product, or firm names in this work is for descriptive purposes only and does not imply endorsement by the authors or their institutions.

References

Alkevli T, Ercanoglu M (2011) Assessment of ASTER satellite images in landslide inventory mapping: Yenice-Gökçebey (Western Black Sea Region, Turkey). Bull Eng Geol Environ 70(4):607–617. https://doi.org/10.1007/s10064-011-0353-z

Antonini G, Ardizzone F, Cardinali M, Galli M, Guzzetti F, Reichenbach P (2002) Surface deposits and landslide inventory map of the area affected by the 1997 Umbria-Marche earthquakes. Boll Soc Geol Ital 121(2):843–853

Ardizzone F, Fiorucci F, Santangelo M, Cardinali M, Mondini AC, Rossi M, Reichenbach P, Guzzetti F (2013) Very-high resolution stereoscopic satellite images for landslide mapping. In: Margottini C, Canuti P, Sassa K (eds) Landslide science and practice. Springer, Berlin Heidelberg, pp 95–101. https://doi.org/10.1007/978-3-642-31325-7_12

Bajracharya B, Bajracharya SR (2008) Landslide mapping of the Everest region using high resolution satellite images and 3D visualization. In: Proceedings of the mountain GIS e-conference, Kathmandu, Nepal, p 14–25

Bartelletti C, Giannecchini R, D'Amato Avanzi G, Galanti Y, Mazzali A (2017) The influence of geological–morphological and land use settings on shallow landslides in the Pogliaschina T. basin (northern Apennines, Italy). J Maps 13(2):142–152. https://doi.org/10.1080/17445647.2017.1279082

Barten PGJ (1999) Contrast sensitivity of the human eye and its effects on image quality. Spie optical engineering press, Bellingham, WA

Bedi SS, Khandelwal R (2013) Various image enhancement techniques- a critical review. IJARCCE 2(3):1605–1609 ISSN (online): 278-1021

Brivio PA, Lechi G, Zilioli E (2006) Principi e metodi di telerilevamento. CittaStudi (ed), Novara

Carrara A, Cardinali M, Guzzetti F (1992) Uncertainty in assessing landslides hazard and risk. ITC J 2:172–183

Casagli N, Fanti R, Nocetini M, Righini G (2005) Assessing the capabilities of VHR satellite data for debris flow mapping in the Machu Picchu area. In: Sassa K, Fukuoka H, Wang F, Wang G (eds) Landslides: risk analysis and sustainable disaster management. Springer, Berlin, pp 61–70. https://doi.org/10.1007/3-540-28680-2_6

Desiato F, Fioravanti G, Fraschetti P, Perconti W, Toreti A (2011) Gli indicatori del CLIMA in Italia nel 2010. ISPRA, Stato dell'Ambiente 24/2011. http://www.isprambiente.gov.it/it/pubblicazioni/stato-dellambiente/gli-indicatori-del-clima-in-italia-nel-2010-anno. ISBN 978-88-448-0499-2 (in Italian). Accessed 27 Aug 2018

Fiorucci F, Cardinali M, Carlà R, Rossi M, Mondini AC, Santurri L, Ardizzone F, Guzzetti F (2011) Seasonal landslides mapping and estimation of landslide mobilization rates using aerial and satellite images. Geomorphology 129:59–70. https://doi.org/10.1016/j.geomorph.2011.01.013

Galli M, Ardizzone F, Cardinali M, Guzzetti F, Reichenbach P (2008) Comparing landslide inventory maps. Geomorphology 94:268–289. https://doi.org/10.1016/j.geomorph.2006.09.023

Guzzetti F, Mondini AC, Cardinali M, Fiorucci F, Santangelo M, Chang KT (2012) Landslide inventory maps: new tools for an old problem. Earth-Sci Rev 112(1):42–66. https://doi.org/10.1016/j.earscirev.2012.02.001

Hackman RJ (1967) Time, shadows, terrain, and photo-interpretation. US Geol Surv Prof Pap 575:155–159

Haeberlin Y, Turberg P, Retière A, Senegas O, Parriaux A (2004) Validation of SPOT 5 satellite imagery for geological hazard identification and risk assessment for landslides, mud and debris flows in Matagalpa, Nicaragua. In: ISPRS, XXth ISPRS Congress Technical Commission I, Istanbul, Turkey, IAPRS, volume 35, part B1, p 273–278. ISSN 1682-1750

Hsieh YT, Wu ST, Liao CS, Yui YG, Chen JC, and Chung YL (2011) Automatic extraction of shadow and non-shadow landslide area from ADS-40 image by stratified classification. In: Geoscience and Remote Sensing Symposium (IGARSS), IEEE International, Vancouver, BC, 24-29 July 2011

Lawrence RL, Ripple WJ (1998) Comparisons among vegetation indices and bandwise regression in a highly disturbed, heterogeneous landscape: Mount St. Helens, Washington. Remote Sens Environ 64:91–102. https://doi.org/10.1016/S0034-4257(97)00171-5

Lee S (2005) Application of logistic regression model and its validation for landslide susceptibility mapping using GIS and remote sensing data. Int J Remote Sens 26(7):1477–1491. https://doi.org/10.1080/01431160412331331012

Lillesand TM, Kiefer RW, Chipman JW (1994) Remote sensing and image interpretation. Wiley, New York ISBN: 978-1-118-34328-9

Liu CC (2015) Preparing a landslide and shadow inventory map from high-spatial-resolution imagery facilitated by an expert system. J Appl Remote Sens 9(1):096080. https://doi.org/10.1117/1.JRS.9.096080

Maini R, Aggarwal H (2010) A comprehensive review of image enhancement techniques. J Comput 2(3):8–13

Marcelino EV, Formaggio AR, Maeda EE (2009) Landslide inventory using image fusion techniques in Brazil. Int J Appl Earth Obs Geoinf 11:181–191. https://doi.org/10.1016/j.jag.2009.01.003

Marchi L, Cavalli M, Comiti F, Vela AL, Viero A (2013) Studio dei processi idrologici, idraulici e geomorfologici e della pericolosità ad essi associata nel bacino del Torrente Pogliaschina (Val di Vara, Provincia della Spezia). Technical report (February 2013), 54 pp, (in Italian)

Mondini AC, Guzzetti F, Reichenbach P, Rossi M, Cardinali M, Ardizzone F (2011) Semi-automatic recognition and mapping of rainfall induced shallow landslides using optical satellite images. Remote Sens Environ 115:1743–1757. https://doi.org/10.1016/j.rse.2011.03.006

Mondini AC, Viero A, Cavalli M, Marchi L, Herrera G, Guzzetti F (2014) Comparison of event landslide inventories: the Pogliaschina catchment test case, Italy. Nat Hazards Earth Syst Sci 14:1749–1759. https://doi.org/10.5194/nhess-14-1749-2014

Moreno RG, Requejo AS, Alonso AT, Barrington S, Díaz MC (2008) Shadow analysis: a method for measuring soil surface roughness. Geoderma 146(1–2):201–208. https://doi.org/10.1016/j.geoderma.2008.05.026

Murillo-García FG, Alcántara-Ayala I, Ardizzone F, Cardinali M, Fiourucci F, Guzzetti F (2015) Satellite stereoscopic pair images of very high resolution: a step forward for the development of landslide inventories. Landslides 12(2):277–291. https://doi.org/10.1007/s10346-014-0473-1

Nichol JE, Shaker A, Wong MS (2006) Application of high-resolution stereo satellite images to detailed landslide hazard assessment. Geomorphology 76:68–75. https://doi.org/10.1016/j.geomorph.2005.10.001

Paine DP, Kiser D (2012) Principles and techniques of aerial image interpretation. In: Paine DP, Kiser JD (eds) Aerial photography and image interpretation, 3rd edn. Copyright © 2012 John Wiley & Sons, Inc., Hoboken, pp 280–305. https://doi.org/10.1002/9781118110997.ch15

Philipson W (1997) The manual of photographic interpretation. American Society for Photogrammetry and Remote Sensing, 2nd edn. American Society of Photogrammetry and Remote Sensing, Bethesda, pp 1–700 ISBN 1570830398 9781570830396

Plank S, Twele A, Martinis S (2016) Landslide mapping in vegetated areas using change detection based on optical and polarimetric SAR data. Remote Sens 8(4):307. https://doi.org/10.3390/rs8040307

Rib HT, Liang T (1978) Recognition, and identification. In: Schuster RL, Krizek RJ (eds) Landslide analysis and control, transportation Research Board special report, 176. National Academy of Sciences, Washington, pp 34–80

Santangelo M, Marchesini I, Bucci F, Cardinali M, Fiorucci F, Guzzetti F (2015) An approach to reduce mapping errors in the production of landslide inventory maps. Nat Hazards Earth Syst Sci 15(9):2111–2126. https://doi.org/10.5194/nhess-15-2111-2015

Schlögel R, Braun A, Torgoev A, Fernandez-Steeger TM, Havenith HB (2013) Assessment of landslides activity in Maily-Say Valley, Kyrgyz Tien Shan. In: Margottini C, Canuti P, Sassa K (eds) Landslide science and practice. Springer, Berlin Heidelberg, p 111–117. https://doi.org/10.1007/978-3-642-31325-7_14

Sun W, Tian Y, Mu X, Zhai J, Gao P, Zhao G (2017) Loess landslide inventory map based on GF-1 satellite imagery. Remote Sens 9(4):314. https://doi.org/10.3390/rs9040314

Temesgena B, Mohammeda MU, Korme T (2001) Natural hazard assessment using GIS and remote sensing methods, with particular reference to the landslides in the Wondogenet area, Ethiopia. Phys Chem Earth 26(9):665–675. https://doi.org/10.1016/S1464-1917(01)00065-4

van Zuidam RA (1985) Aerial photo-interpretation in terrain analysis and geomorphologic mapping International Institute for Aerospace Survey and Earth Sciences (ITC). Smits Publishers, The Hague, p 442

Weirich F, Blesius L (2007) Comparison of satellite and air photo based landslide susceptibility maps. Geomorphology 87:352–364. https://doi.org/10.1016/j.geomorph.2006.10.003 http://www.planar.com/media/211324/mn-planar-sd2020.pdf. Accessed 27 Aug 2018

F. Fiorucci · F. Ardizzone (✉) · A. C. Mondini · F. Guzzetti
Consiglio Nazionale delle Ricerche,
Istituto di Ricerca per la Protezione Idrogeologica,
via della Madonna Alta 126, I-06128, Perugia, Italy
Email: francesca.ardizzone@irpi.cnr.it

A. Viero
Private Consultant, Padova, Italy. Formerly Consiglio Nazionale delle Ricerche,
Istituto di Ricerca per la Protezione Idrogeologica,
Corso Stati Uniti 4, I-35127, Padova, Italy